ADVANCED MATERIALS
www.advmat.de

Bioinspired Nanoscale 3D Printing of Calcium Phosphates Using Bone Prenucleation Clusters

Iman Roohani, Shuning Wang, Chaohui Xu, Peter Newman, Ali Entezari, Yichen Lai, and Hala Zreiqat**

Calcium phosphates (CaPs) are ubiquitous in biological structures, such as vertebrate bones and teeth, and have been widely used in biomedical applications. However, fabricating CaPs at the nanoscale in 3D has remained a significant challenge, particularly due to limitations in current nanofabrication techniques, such as two-photon polymerization (2pp), which are not applicable for creating CaP nanostructures. In this study, a novel approach is presented to 3D print CaP structures with unprecedented resolution of ≈300 nm precision, achieving a level of detail three orders of magnitude finer than any existing additive manufacturing techniques for CaPs. This advancement is achieved by leveraging bioinspired chemistry, utilizing bone prenucleation nanoclusters (PNCs, average size of 5 nm), within a photosensitive resin. These nanoclusters form a highly transparent photoresist, overcoming the light-scattering typically associated with larger calcium phosphate-based nanoparticles. This method not only allows for nanopatterning of CaPs on diverse substrates, but also enables the precise control of microstructure down to the level of submicron grains. The method paves the way for the developing of bioinspired metamaterials, lightweight damage-tolerant materials, cell-modulating interfaces, and precision-engineered coatings.

1. Introduction

The repair of bone defects caused by trauma, infection, tumors, or congenital malformations, remains a significant clinical challenge. Autologous bone grafting, which involves harvesting bone from the patient, remains the gold standard for bone defect repair.[1,2] This is a highly effective technique because autologous bone can directly bond with the host skeleton (osteoconduction) and stimulate local stem cells to differentiate into bone-forming cells (osteoinduction) without provoking adverse immune responses. However, autologous bone grafting also has major drawbacks, including limited bone supply, donor site morbidity, and an increased risk of infection, necessitating the development and use of alternative bone grafting materials.[1]

CaPs are widely used materials to create synthetic bone grafts to replace or minimize the use of autologous grafts. Their chemical similarity to bone mineral, coupled with their biocompatibility and bioactivity makes CaPs attractive candidates for bone regeneration.[3–9] Despite their widespread application, CaPs are currently limited to repairing small, non-load-bearing bone defects due to their brittleness, low mechanical strength, and limited osteoinductive properties.[10–13] The primary challenge lies in their lack of inherent osteoinductivity; the ability to recruit mesenchymal stem cells and induce their differentiation into the osteogenic lineage.[10–13]

Recent evidence suggests that the osteoinductive properties of CaPs are closely linked to their micro- and submicron-scale structural features, including microporosity (pores smaller than 10 µm) and pore curvature.[14–20] These features have been identified as critical factors influencing the osteoinductivity of CaPs. To date, various fabrication techniques, including freeze-drying, microsphere sintering, gas foaming, and 3D printing, have been developed to introduce pores in CaPs.[21] However, these techniques face significant limitations to precisely control the size, shape, depth, distribution, and arrangement of micropores.[21,22] Consequently, no quantified or robust consensus exists regarding the specific configuration of micropores or submicron-scale features that induces, if at all, osteoinduction.[23,24] Even if such parameters were identified, current techniques cannot systematically and reproducibly incorporate these microstructural

I. Roohani, S. Wang, C. Xu, P. Newman, A. Entezari, Y. Lai, H. Zreiqat
School of Biomedical Engineering
University of Sydney
Sydney, NSW 2006, Australia
E-mail: hala.zreiqat@sydney.edu.au
I. Roohani, A. Entezari
Lab of Advanced Biomaterials and Fabrication
School of Biomedical Engineering
Faculty of Engineering and Information Technology
University of Technology Sydney
Sydney, NSW 2007, Australia
E-mail: iman.roohani@uts.edu.au
P. Newman
EMBL Australia
Single Molecule Science node
School of Biomedical Sciences
University of New South Wales
Sydney, NSW 2052, Australia
The ORCID identification number(s) for the author(s) of this article can be found under https://doi.org/10.1002/adma.202413626

DOI: 10.1002/adma.202413626

features into CaP-based bone grafts. This technological gap has led to inconclusive and often contradictory results regarding the role of microporosity in osteoinduction. Nanoscale printing of CaPs presents an unprecedented opportunity to overcome these limitations. This approach enables the precise fabrication of arbitrarily designed micropores and nanoscale surface features, allowing for the systematic investigation of the mechanisms underlying osteoinduction in CaPs. Such advances could yield reproducible, osteoinductive CaPs capable of reliably bridging critical-sized bone defects; an achievement that remains unattainable with current CaP ceramics.

Another critical limitation of traditionally fabricated CaPs, is their low mechanical strength.[13,25] The presence of stochastic flaws, such as microscale cracks that act as stress concentrators within the microstructure, is the primary contributor to the low strength of ceramics including CaPs. Despite years of research, attempts to improve the mechanical properties of CaPs have been only partially successful. Previous efforts have focused primarily on compositional modifications aimed at impeding or deflecting crack propagation, but these have not produced substantial gains in strength or toughness. Ceramics can achieve flaw insensitive behavior when their dimensions are reduced below a critical size (typically submicron), causing their strength to approach the theoretical limit.[26–29] Under such conditions, strength values can be orders of magnitude higher than experimental values, and ceramic structures may even exhibit elasticity. However, this architectural approach to enhancing the mechanical properties of CaPs remains unexplored due to the limitations of current CaPs fabrication techniques, which cannot produce complex porous architectures at the submicron scale.

Nanoscale 3D printing of CaPs enables the fabrication of solid parts with submicron dimensions that are either free of flaw or contain flaws that are orders of magnitude smaller than those found in CaPs fabricated through traditional top-down approaches. As a result, such structures can approach theoretical strength values and exhibit improved deformability through scale-independent architectures (e.g., nano-latticing). These architectures accommodate larger displacements and endure greater elastic strains due to increased yield strengths.[29,30] By enabling the nanoscale design and construction of CaP scaffolds this technology opens the door to using CaPs in load-bearing bone defects; an area that has remained largely inaccessible to conventional fabrication methods

Over the past decades, several approaches have been developed for fabricating CaP structures with intricate geometries and controlled micro-to nanoscale features. These approaches include template-directed methods, such as chemical mineralization in nanoporous templates, which enable the design of mineralized CaP nano-constructs through spatial confinement.[31,32] Another example of template-directed techniques is enzyme-assisted mineralization, where controlled reactions within confined environments provide precise regulation of crystallinity and structural anisotropy in the resulting CaP constructs.[33] Although these techniques provide unique advantages, such as enabling the incorporation of biomacromolecules such as collagen to mimic mineralized extracellular matrices, they are inherently constrained by the use of templates, which limit geometric flexibility and true 3D spatial control in fabrication.

In contrast, advancements in additive manufacturing technologies have introduced unprecedented flexibility for fabricating CaP structures with complex and 3D geometries, overcoming many of the constraints of traditional methods.[34–36] However, the minimum feature size achievable for CaP constructs using current additive manufacturing techniques remains at ≈120 µm. While nanoscale spatial resolution can be attained via 2PP, this technique is predominantly employed for organic materials, as it requires high transparency in precursors to avoid light scattering.[37–42]

Significant progress has recently been made in the micro- and nanoscale 3D printing of ceramics, glasses, and metals using 2PP. These approaches can be broadly classified into indirect and direct methods.[30,42–45] Indirect approaches primarily rely on the use of organic templates created via 2PP, which are subsequently coated with a ceramic layer and subjected to sintering.[46,47] However, these methods are less versatile than direct approaches due to their dependence on organic templates, the limited range of ceramics that can be effectively coated, and the constraints on template designs, which must ensure uniform and efficient ceramic deposition. Direct approaches can be categorized into methods employing 2PP photocurable ionic solutions of metal oxides,[48–51] photocurable hydrogels embedded with inorganic nanoparticles,[52] and utilizing preceramic monomers.[30,42–45] These approaches typically lead to substantial shrinkage after calcination (e.g., up to thirteen-fold for hydrogel-based) and are often unsuitable for ceramics that react with aqueous media. Applying direct 2PP techniques to CaPs, particularly those based on aqueous systems, presents several challenges. CaP nanoparticles, such as amorphous calcium phosphate (ACP) and hydroxyapatite (HA), react rapidly with water, resulting in increased particle size and crystallinity. This reactivity leads to significant light scattering and a consequent reduction in print resolution. Furthermore, techniques that rely on ionic solutions with precise calcium-to-phosphorus ratios face additional obstacles, as these ions tend to precipitate and agglomerate quickly, further complicating the fabrication process. Another direct approach, primarily employed for metal constructs, utilizes well-dispersed metallic nanoclusters within 2PP photosensitive resins to address the light-scattering challenges associated with larger nanoparticles.[53–55] Inspired by the effectiveness of nanoclusters in minimizing light scattering, this study pioneers a novel approach that, for the first time, harnesses the capabilities of 2PP to achieve 3D printing of CaP structures with an unprecedented resolution of ≈300 nm.

2. Results and Discussion

For this purpose, we utilized PNCs as the main component of the resin formulation. PNCs represent nanoscale transient calcium phosphate species that play a critical role in early biomineralization processes specifically found during bone formation, acting as intermediates between dissolved ions and solid mineral phases.[56–64] These clusters, typically composed of sub-nanometric to nanometric calcium triphosphate ions ($Ca(HPO_4)_3^{4-}$), are precursors to ACP granules, which eventually transform into thermodynamically stable crystalline HA during bone formation.[56,65–67] In this study, we successfully synthesized amorphous PNCs with a median size of 5 nm

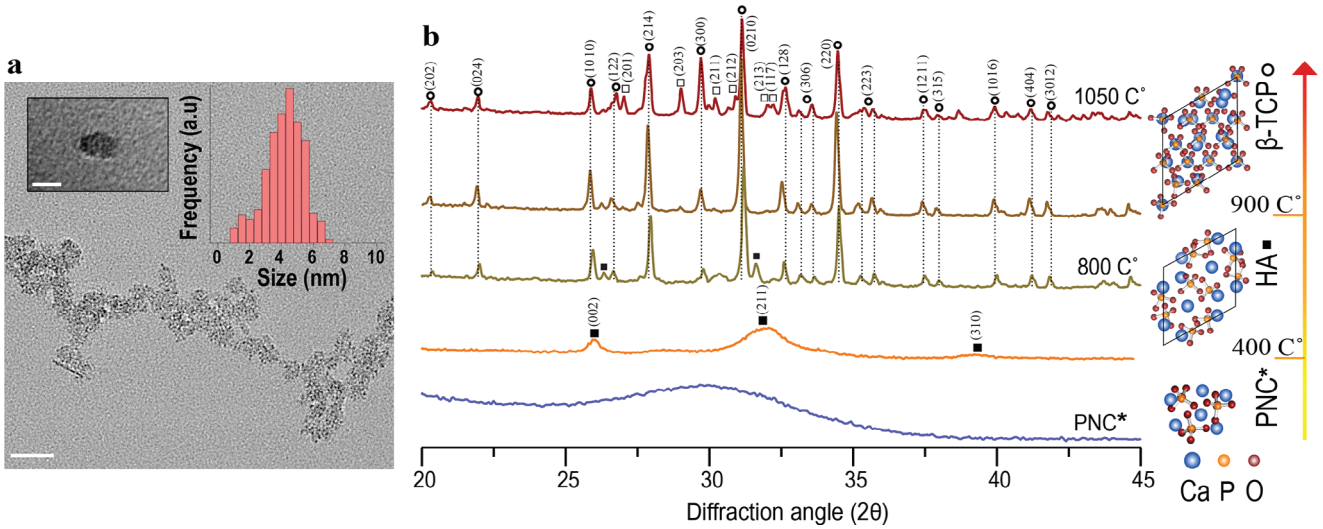

Figure 1. Synthesis of PNCs and their thermal transformation into calcium phosphate phases. a, transmission electron microscopy (TEM) image of typical morphology of the PNCs showing average diameter of 5 nm (scale bar, 20 nm, inset scale bar; 5 nm). b, XRD pattern of PNCs demonstrating an amorphous structure (blue line), and PNCs heat treated heat treated at 400, 800, 900, and 1050 C° for 1 h, demonstrating increasing the crystallinity and formation of HA at lower temperatures and transition to β-TCP and β-calcium pyrophosphate (β-Ca2P2O7) at higher temperatures under ambient condition. The (*) indicates that the XRD pattern of PNC represents the dried sample, which has transitioned into ACP (Figure S1, Supporting Information).

(**Figure** 1a). The PNCs demonstrated the ability to transform into various CaP phases through heat treatment under ambient conditions (Figure 1b).

The dried PNCs exhibited an amorphous structure, as confirmed by the absence of sharp peaks in their XRD pattern. Upon heat treatment at 400 °C, a semi-crystalline HA phase began to form, evidenced by the appearance of broad peaks. Increasing the temperature to 1050 °C led to the formation of crystalline β-TCP (β-tricalcium phosphate) and β-calcium pyrophosphate. However, PNCs inherently tend to agglomerate and rapidly transform into ACP, which eventually crystallizes into HA at room temperature (Figure S2, Supporting Information). Achieving nanoscale resolution in 3D printing of CaPs hinges on the stabilization of these PNCs to prevent their inherent tendency to agglomerate and transform into crystalline phases. To address this challenge and stabilize colloidal PNCs, the clusters were functionalized with triethylamine, resulting in non-agglomerating nanoparticles as seen in the TEM micrograph (Figure 1a). It is noteworthy that PNCs stored at room temperature for two weeks (Figure S2, Supporting Information) exhibit higher crystallinity compared to those subjected to heat treatment at 400 °C (Figure 1b). This phenomenon is attributed to solution-mediated crystallization under equilibrium conditions, which facilitates well-ordered HA crystal growth. In contrast, heat treatment at 400 °C induces solid-state phase transformations under non-equilibrium conditions, where limited ion diffusion and restricted atomic rearrangement result in lower crystallinity.

Stabilized PNCs were subsequently embedded and homogenized in a photoresin to create a 2PP-compatible ink. To ensure consistency across experiments and minimize the impact of the photopolymer on the results, the commercially available IP-L, an acrylate-based resin that cures via a free-radical polymerization mechanism, was selected. The resulting photocurable ink (PNC ink) was a clean, transparent, light-yellow solution (**Figure** 2a), with the PNCs retaining their amorphous state throughout the incorporation process. Notably, any destabilization or partial crystallization of the PNCs caused the ink to become instantly opaque (Figure S3, Supporting Information), highlighting the importance of maintaining colloidal stability during the formulation. For 2PP printing, the PNC ink was successfully employed in both dip-in and immersion modes, demonstrating adaptability to a variety of substrate requirements (Figure 2b). In immersion mode, suitable for opaque substrates such as titanium alloys, silicon wafers, and alumina, the objective lens was immersed directly into the PNC ink, with printing progressing in the negative z-axis direction from the substrate interface. Conversely, the dip-in mode enabled printing through transparent substrates such as fused silica, proceeding in the positive z-axis direction. These distinct configurations allowed for a versatile and precise fabrication process tailored to specific substrate types. Using the transparent PNC ink, we achieved 3D printing of CaP structures at an unprecedented nanoscale resolution using 2PP (Figure 2c). This approach enabled the fabrication of 10 000 CaP grains, each measuring ≈320 nm in diameter and ≈380 nm in height, printed on a fused silica substrate over an area of 200 µm × 200 µm, with uniform spacing of 2 µm between grains. Moreover, continuous nanoscale features, such as a uniformly printed line with a consistent diameter of ≈290 nm, were fabricated (Figure 2c, bottom panel). These results highlight a remarkable advancement, achieving spatial resolution that surpasses previous 3D printing techniques for CaPs by more than two orders of magnitude. Beyond the creation of discrete submicron-grain structures, this method facilitates the precise fabrication of continuous nanoscale features, establishing a new benchmark for the resolution and scalability of 3D-printed CaP constructs.

The sub-micrometer 2PP 3D printing of ceramics heavily depends on ceramic-photopolymer inks with high optical

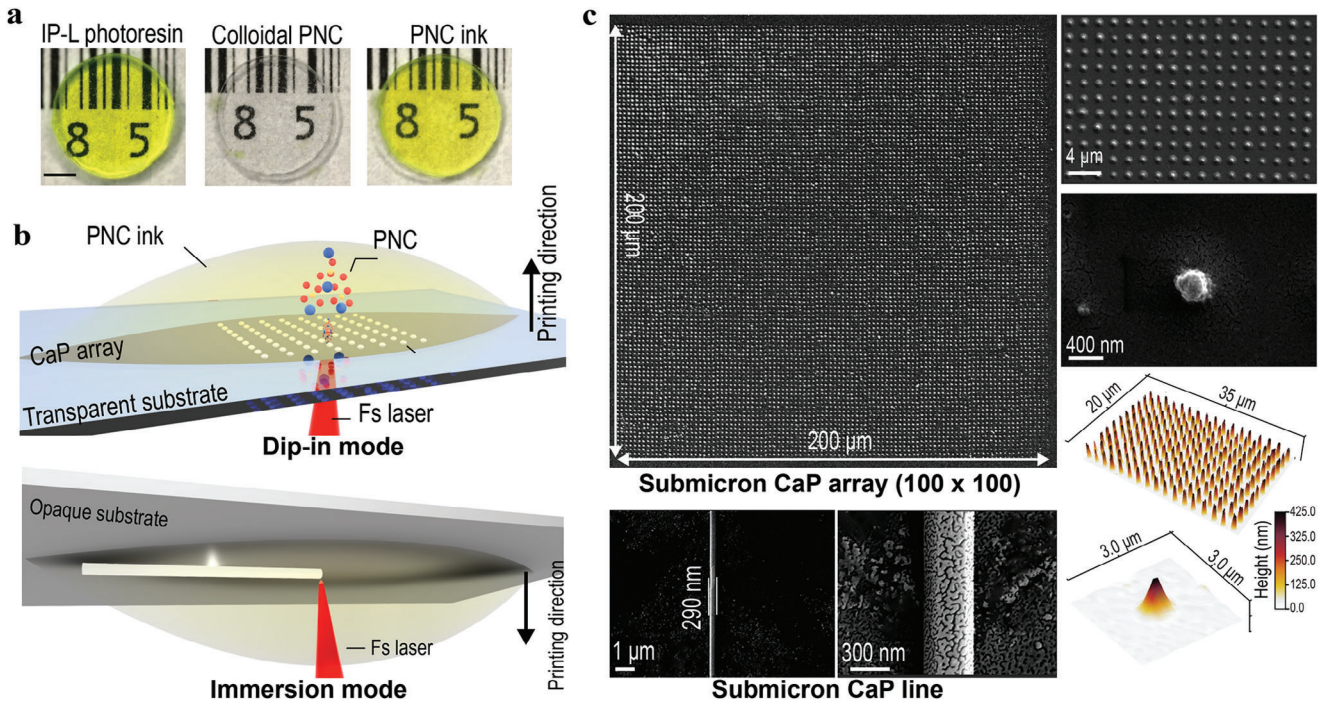

Figure 2. Developing a CaP photoresist with bioinspired chemistry and process of 2pp-enabled 3D printing of CaP nanostructures. a) photographs of the IP-L photoresin, the colloidal PNCs and the homogenized PNC ink (40 wt.%) (scale bar: 3 mm). b) schematic of 2PP-enabled 3D printing set-up (dip-in and immersion modes) and printing process of discontinuous CaP array and CaP submicron line. c) Scaning electron microscopy (SEM) images of array of 100 × 100 CaP submicron-grains printed uniformly in a 200 µm × 200 µm area, and a single line with an average diameter of ≈290 nm.

transmittance. This transmittance is inversely correlated with ceramic particle size: smaller particles scatter less light, thereby enhancing transmittance essential for effective 2PP. The PNC ink, with a concentration of up to 80 wt.% of PNCs, achieves an impressive 85% transmittance at an 800 nm wavelength through a 100 µm light path. This represents a significant advancement compared to inks containing HA nanoparticles (average size of 85 nm) and ACP particles (average size of 50 nm), which exhibit transmittance below 40% even at much lower concentrations (5 wt.%) (**Figure** 3a).

Small-angle X-ray scattering (SAXS) analysis on PNC inks confirms that PNCs are uniformly dispersed within the polymer matrix, showing no signs of particle agglomeration after mixing and homogenization (Figure 3b). The particle size distribution closely aligns with the 1–10 nm range observed in TEM images. Further investigations reveal that, under femtosecond laser irradiation, PNCs transform into spherical ACP particles, evidenced by the formation of spherical CaP entities ranging from 40 to 280 nm in diameter in both as-printed and calcined samples (Figure S4, Supporting Information). We hypothesize that during the 2PP 3D printing process, PNCs coalesce into larger, spherical ACP-like particles under laser irradiation without altering their crystallinity (see Figure S5, Supporting Information). This coalescence may occur either during or after irradiation, driven by the inherent instability of PNCs, which leads them to merge into thermodynamically stable forms over time. The later-stage transient ACP commonly appears hollow due to its dissolution-recrystallization behavior during transformation into HA. This process involves surface dehydration and crystallization, forming a stable outer layer, while the hydrated interior dissolves due to diffusion-driven water loss and interaction with the surrounding medium. Surface crystallization then acts as a barrier, focusing dissolution within the particle's core, resulting in hollow structures.[68] This phenomenon results in a size increase of four to ten times the original diameter, forming mature ACP-like nanoparticles. To validate this hypothesis, synthesized PNCs were subjected to femtosecond laser irradiation, followed by structural analysis using cryo-TEM. The TEM results corroborate our hypothesis, showing the transformation of PNCs into ACP particles post-irradiation (Figure 3c). While these observations align with previously reported trends, the dynamics of coalescence and specific changes to their state remain unclear and require further investigation. We emphasize that this proposed mechanism represents a conceptual interpretation of the transformation process, and additional techniques, such as cryo-TEM, would be needed to provide more definitive insights into the colloidal state and evolution of PNCs.

Figure 4 showcases the versatility of 2PP in fabricating CaP lattice structures and patterns with the PNC ink. Figure 4a illustrates the technique's ability to create intricate, scalable cellular structures ranging from macro to nanoscale. These include a gyroid lattice with dimensions of 250 µm × 50 µm × 250 µm and a wall thickness of 850 nm, down to a much smaller structure: a 3 × 3 × 3 octet lattice truss structure, featuring a unit cell size of 2 µm × 2 µm × 2 µm and struts size of 360 nm. The shrinkage of the constructs after sintering is between 15% and 35%, depending on the amount of PNCs in the IP-L and the sintering temperature. This shrinkage is relatively minor compared to

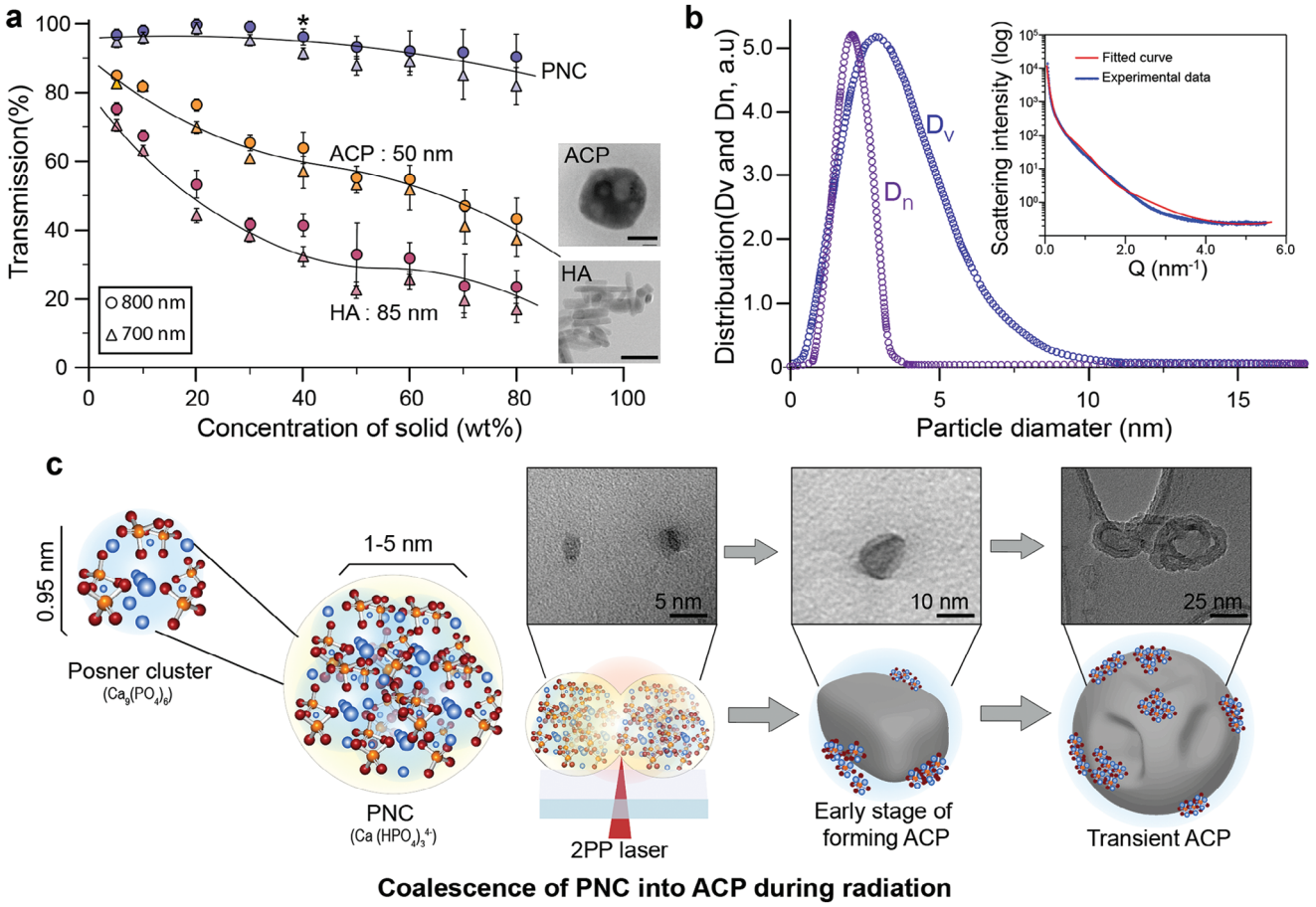

Figure 3. Optical properties of PNC ink and coalescence of PNCs.a) Transmittance of cured photopolymer with increasing mass loading of PNCs, ACP, and HA nanoparticles demonstrating high transmittance across a large weight fraction range for PNC inks, for two wavelengths of the incident light 700 and 800 nm. Size of the Scale bar for TEM of ACP is 20 nm and for HA is 100 nm. b) Particle diameter distribution of PNCs from SAXS-measurements of the photopolymer ink with 40 wt.% mass loading at 100 µm layer thickness. c) Schematic of interaction of PNCs with femtosecond laser resulting in coalescence of clusters into early stage of forming ACP (n = 3, $^{*}p$ <0.05).

other vat-photopolymerization techniques highlighting the structural support provided by the high PNC concentration. However, sintering above 1050 °C led to significant deformations and structural collapse due to thermal expansion mismatches. However, sintering above 1050 °C leads to significant deformations and structural collapse due to thermal expansion mismatches and excessive shrinkage during sintering, particularly for intricate structures. To mitigate this, we designed support structures to accommodate differential thermal expansion and shrinkage experienced during the sintering process (Figure S6, Supporting Information). These supports absorb the stresses that would otherwise lead to deformation or collapse. In addition to structural measures, increasing the density of printed structures before sintering could provide further solutions to mitigate shrinkage while improving mechanical stability. When films made from PNC ink were immersed in simulated body fluid, they became opaque due to the extensive formation of apatite crystals (Figure S7, Supporting Information), confirming the reactivity of the PNCs. This reactivity could be strategically exploited to enhance the densification of structures post-printing, potentially reducing shrinkage after sintering. Furthermore, the ability of PNCs to react with additional elements offers opportunities to deliberately introduce a range of bioactive elements into the PNC structure, tailoring the biological function of constructs.[69] Furthermore, energy-dispersive spectroscopy mapping confirmed the uniform distribution of calcium and phosphorus elements in the sintered PNC structures (Figure S8, Supporting Information). The scalability of our approach is further demonstrated by seeding the octet lattices with induced pluripotent stem cells (iPSCs), where a single iPSC cell is nearly twice the size of the CaP construct's unit cell, highlighting the precision in nanoscale fabrication (Figure S9, Supporting Information). The 2PP technique using PNC ink enables precise control over the microstructure of CaP constructs, including grain number, size and spacing. This is achieved through adjustable printing parameters including laser slicing distance, voxel aspect ratio, and hatching distance as well as sintering temperature and time, which facilitate a precise manipulation of the microstructure (Figure S10, Supporting Information). Figure 4b-i demonstrates this in a microscale inscription of "Materials", where each letter across the inscriptions comprises a consistent number of discrete grains, each ≈1 µm thick. Additionally, "Nano" is inscribed at varying scales.

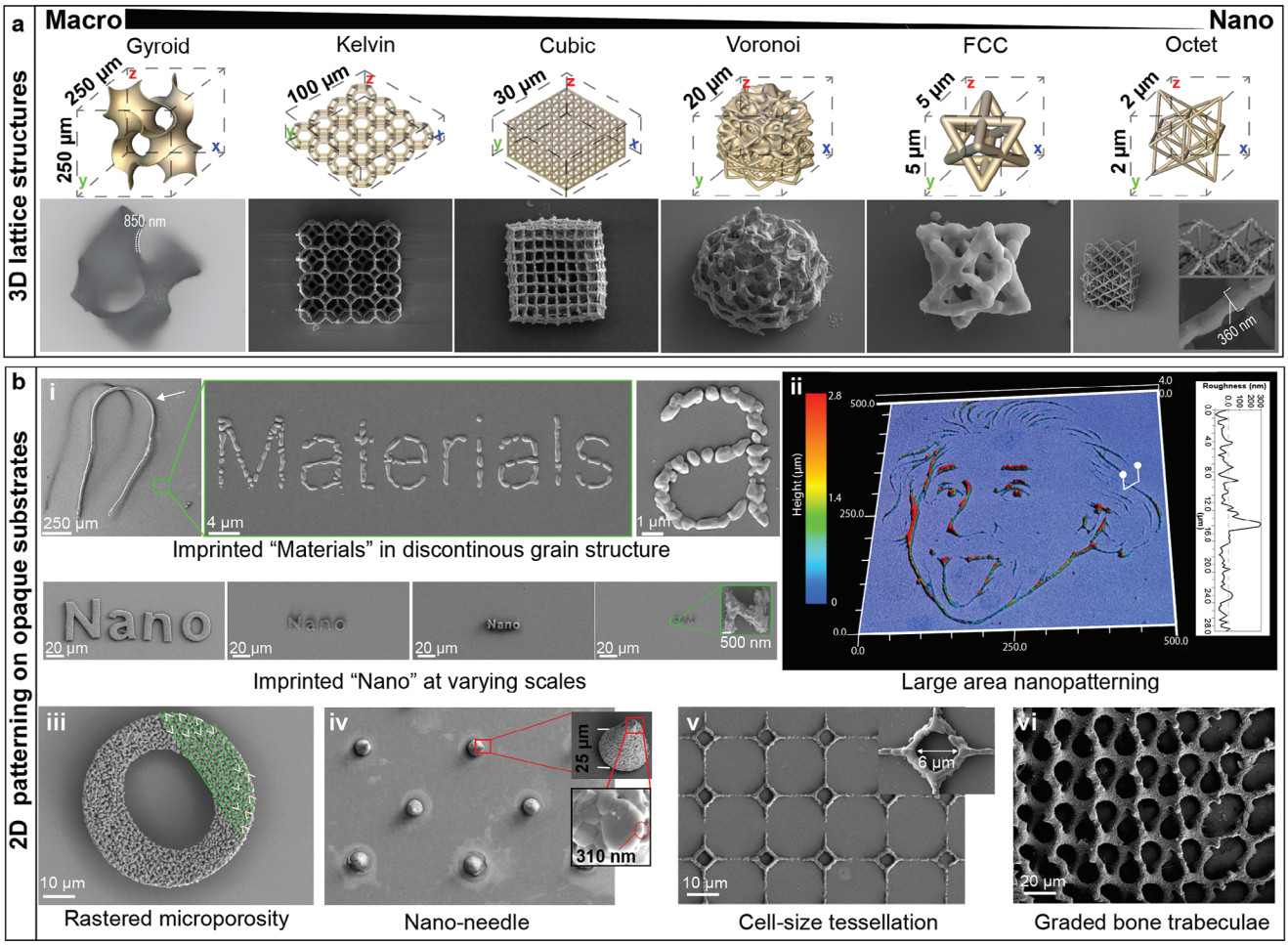

Figure 4. CaP 3D lattice structures and patterns printed using the PNC ink. a) Models and SEM micrographs displaying a progression of 2PP-printed lattice structures from macro to nano scales. Structures include: Gyroid (optical image, 250 µm × 250 µm × 250 µm), Kelvin (100 µm × 100 µm × 25 µm), Cubic (30 µm × 30 µm × 12 µm), Voronoi (20 µm × 20 µm × 20 µm), FCC (5 µm × 5 µm × 5 µm) and Octet (unit cell size of 2 µm × 2 µm × 2 µm). b) Nanopatterning on opaque substrates: i) Microscale inscription of "Materials" and "Nano" next to a human hair (arrow) for scale. Each letter consists of arbitrary placed bicontinuous grains with consistent number of granular pockets in all patterns; ii) A large-area (500 µm × 500 µm) representation of Einstein's face demonstrating surface roughness variations from 2.8 to 300 nm; iii) Rastered microporosity within a single "O" letter achieved by varying laser raster spacing; iv) An array of nano-needles showcasing a tip radius of 310 nm and base diameter of 25 µm; v) Uniform, single-cell tessellation with 6 µm diameters and double grain height; vi) Biomimetic sub-micron patterning emulating bone trabeculae.

Moreover, this technique is capable of precise nano/micropatterning of opaque surfaces. Figure 4b-ii demonstrates its ability to replicate Einstein's face across a 500 µm × 500 µm area, creating micro-nano topography on a silicon wafer. Further, Figure 4b-iii highlights the method's success in generating controlled microporosity within a single "O" letter, a crucial microstructural niche for enhancing osteogenic properties of scaffolds in bone tissue engineering, a capability previously unattainable with existing fabrication technologies.[70–72] Moreover, Figure 4b-iv presents the first instance of an array of CaP nanoneedles, characterized by a tip radius of 310 nm and a base diameter of 25 microns. This feature demonstrates the technique's potential for applications ranging from cellular manipulation to targeted drug delivery.[73,74] Figure 4-v,vi highlights the use of 2PP in biomimetic sub-micron patterning, including single-cell tessellation and emulating bone trabeculae. This technique offers remarkable design flexibility for fabricating bioinspired hierarchical structures. Current additive manufacturing techniques fail to capture the nuanced micro- and nano-scale architectures critical for achieving the functional properties of biological structures, particularly for complex multiscale structures made from inorganic materials.[75] **Figure 5a** shows a microfabricated Bouligand structure, comprises continuous unidirectional CaP fiber sheets helically stacked with 30° rotation angle between adjacent fiber layers. The fibers, each 2 µm in diameter and spaced 1 µm apart, mimic the energy-absorption structure commonly found in biological materials, such as lobster claw, which help resist dynamic loading.[76] Figure 5b,c demonstrate the first detailed examples of bone tissue mimicked structures: i) a bone micro tissue containing two levels of hierarchy of concentric rings of fibrils (d = 1 µm) forming osteons (d = 22 µm) and harversian channels (d = 5 µm), interface between cortical and cancellous bone with trabeculae thickness of 650 nm. ii) a thin histological section of

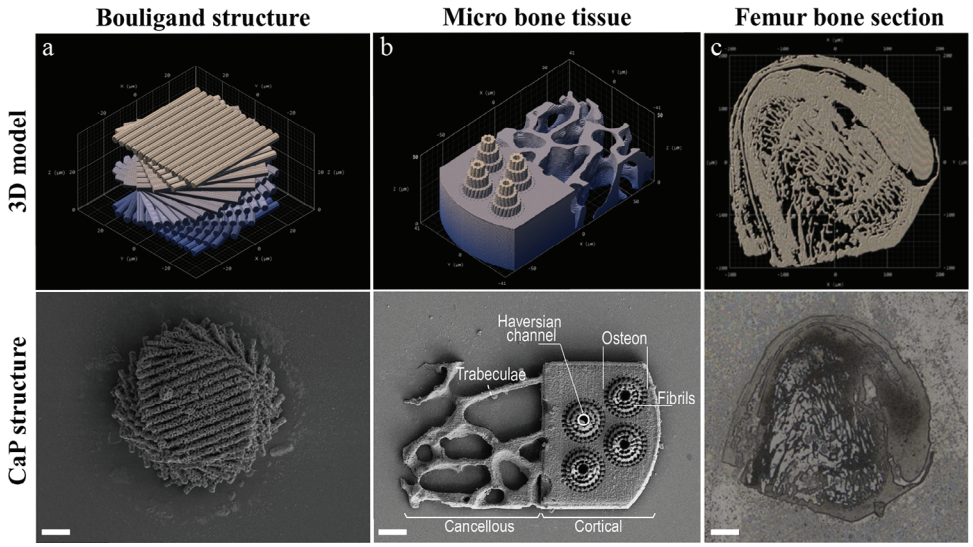

Figure 5. 2PP-enabled CaP biomimetic structures. Biomimetic CaP structures fabricated using PNC ink. a) Engineered Bouligand structure designed to allow lamellar reorientation akin to load-responsive mechanisms observed in various natural materials (scale bar, 10 µm). b) Scaled 1:20 of a micro bone tissue displaying osteons, Haversian channels, and concentric rings of oriented fibrils as well as an interface transition of nanothin trabecular bone to cortical bone, (scale bar, 10 µm). c) Scaled 1:100 representation of a histological section of a femur bone, demonstrating the larynx of trabecular bone with varying plate thickness (scale bar, 50 µm).

femur bone preserving high details of fine trabeculae and cortical compartments.

In summary, we have demonstrated the first example of nanoprinting of CaPs by utilizing a bioinspired chemistry that incorporates PNCs into a photoresist. The success of our technique hinges on two key factors: i) the stabilization of PNCs with particle sizes smaller than 10 nm to achieve nanoscale resolution, and ii) the use of homogeneous 2PP inks (Figure S11, Supporting Information) containing a high mass of PNCs to maintain print geometry of the printed structure and minimize deformation during cleaning and sintering. This innovative approach has resulted in a high transmissive photoresist capable of supporting the nanoprinting of complex CaP nanoarchitectures that were previously unattainable.

The nanoscale 3D printing of CaP structures presented in this study marks a significant breakthrough; however, certain limitations must be acknowledged. A key constraint is the need for post-printing sintering and calcination at elevated temperatures, which prevents the direct incorporation of heat-sensitive biomacromolecules, such as proteins or growth factors, and living cells during the fabrication process. Nevertheless, biological components can be introduced post-sintering through surface functionalization techniques, including chemical grafting, adsorption, or hydrogel infiltration. Furthermore, the prenucleation clusters demonstrated in this work hold significant potential for integration with biocompatible resins or hydrogels, providing an opportunity to create hybrid structures that mimic mineralized extracellular matrices such as bone while retaining biological functionality.

Another limitation is the trade-off between nanoscale resolution and printing speed, particularly when fabricating larger constructs. While one of the technique's main advantages is its ability to achieve exceptionally fine detail, producing larger constructs at the nanoscale is time-consuming. This limitation is intrinsic to current multi-photon lithography technologies. However, future advancements, such as faster scanning systems and optimized fabrication workflows—may address scalability concerns.

Moreover, although this study successfully demonstrates the capability to fabricate nanoscale CaP constructs, it does not provide a detailed assessment of their mechanical properties. This level of precision provides a promising foundation for exploring structures with unique properties and functionalities, such as ultra-lightweight materials with enhanced stiffness, deformability, and recoverability through nanolatticing.[29,46] While this concept has been demonstrated for metals, polymers, and certain ceramics, its application to CaP remains speculative and requires future validation to confirm its feasibility and scope.[29,46]

Given the well-established relationship between microstructure and mechanical performance in ceramics, the precise control enabled by nanoscale 3D printing offers significant potential for mechanical enhancements. By minimizing stochastic flaws and enabling hierarchical architectures, nanoscale 3D printing demonstrates potential for significant improvements in mechanical properties, including enhanced toughness, flaw tolerance, and deformability. However, achieving these improvements fully requires careful optimization of the microstructure to minimize defects, as well as precise control of the grain size-to-flaw ratio. These refinements are critical to approaching theoretical strength values and overcoming the challenges observed in the current study. The technique introduced here provides a powerful platform for fabricating nanoscale CaP structures with unprecedented control over microstructural features. This capability not only enables systematic studies to explore the relationship between microstructure and material properties but also lays the foundation for developing next-generation CaP-based materials with enhanced biological and mechanical functionalities.

3. Experimental Section

Calcium chloride dihydrate ($CaCl_2 \cdot 2H_2O$), 99.0%), phosphoric acid (H_3PO_4, ≥85 wt. % in H_2O), ethanol (C_2H_5OH, 99.7%), propylene glycol monomethyl ether acetate (PGMEA, $CH_3CO_2CH(CH_3)CH_2OCH_3$, ≥99.5%), triethylamine ($(C_2H_5)_3N$, 99.9%), isopropanol alcohol (C_3H_8O, ≥99.5%), glacial acetic acid (CH_3COOH, ≥99.8%), 3-(Trimethoxysilyl) propyl methacrylate ($C_{10}H_{20}O_5Si$, ≥99.8%), and ethylenediaminetetraacetic acid disodium salt dihydrate (EDTA, $C_{10}H_{14}N_2Na_2O_8$, ≥99.0%) were purchased from Sigma-Aldrich. IP-L, a liquid resin (viscosity: 890 mPa s at 20 °C, refractive index: 1.485 at 589 nm, 20 °C) was purchased from Nanoscribe. Two-sided polished sapphire and fused silica substrates with 100 µm thickness were purchased from University Wafer (Florida, USA). HPSI0314i-hoik_1 hiPSC line obtained from Wellcome Sanger Institute with the help of Cell Bank Australia. Essential 8 Flex media (E8F) and CEPT cocktail were purchased from Thermo Fisher Scientific.

Preparation of PNC Ink: A solution containing calcium ions (16.3 mM) was prepared by dissolving calcium chloride in ethanol and triethylamine solution (volume ratio of 40:1.9). The phosphate containing solution was prepared by addition of 70 µL of phosphoric acid into 20 mL of ethanol. Upon mixing the solutions in a dropwise manner, gel-like PNCs formed and were then separated by centrifuging at 4400 rpm for 2 min. The gels were placed in a vacuum drying chamber at ambient room temperature for 30 min, facilitating solvent evaporation. Subsequently, they were either immediately stored in a −20 °C freezer within sealed Falcon tubes or utilized for ink preparation. The dried PNC gels were initially hand-mixed with IPL resin, and this mixture was then transferred to zirconia-coated stainless-steel jars. These jars contained yttria-stabilized zirconia balls, each with a diameter of 5 mm. For homogenization, the PNC inks underwent processing in a planetary ball mill (Model PM 400, Retsch, Germany) for a duration of 4 h at a speed of 150 rpm. The stages of this homogenization process are shown in the supporting information (Figure S10, Supporting Information).

2PP 3D-Printing of CaP: The surface of substrates used in oil-immersion mode were silanized to enhance the adhesion of prints to substrates. For silanization, fused silica substrates were washed with ethanol three times and cleaned in an ultrasonic cleaner in a methanol bath for 2 min. They were then transferred into a beaker containing 100 mL methanol, 5 mL acetic acid, and 3 mL of 3-(Trimethoxysilyl) propyl methacrylate and incubated for 45 min. After incubation, substrates were removed from the beaker and washed with methanol three times followed by rinsing using ethanol and stored in a desiccator. The surface of opaque substrates (e.g., silicon wafer and titanium alloy) were cleaned with O_2 plasma treatment prior to printing. The 2PP printing was performed by Nanoscribe Photonic Professional GT2. In the oil-immersion mode, a 63× objective lens with a numerical aperture (NA) of 1.4 was utilized, whereas a 25× objective lens with an NA of 0.8 was selected for the Dip-in mode to facilitate the printing process. During oil-immersion, PNC ink was applied onto a fused silica substrate, which was then positioned in the Nanoscribe substrate holder. The photon dose – the laser energy per unit area – was finely tuned through adjustments in PowerScaling (a multiplier for the overall laser power), LaserPower (variable from 0 to 100%), and ScanSpeed (the laser focus velocity during printing), as specified in the GWL file via Describe software. Designs exceeding 30 µm in height were segmented into blocks with varying laser power and scan speed. The same procedure used for dip-in mode, except PNC ink was added on the objective lens. After the printing process, the substrates were immersed in EDTA (10 wt.% in Milli-Q water) for 1 min to remove the unreacted PNCs and then immersed in Milli-Q water followed by quickly dipping into in PGMEA to dissolve the unpolymerized precursor.

Heat-Treatment Process: Heat treatment in an electric furnace under atmospheric ambiance was performed for removing the organic components and sintering of prints. A detailed temperature-time schedule for calcination can be found in supporting information figures (Figure S12, Supporting Information). Structures were treated at holding temperatures of 400, 600, 800, 900, 1000, 1050, 1100, and 1200 °C for a duration of 3h. At the end of sintering schedule samples were kept in the furnace in cooling phase to slowly return to room temperature to minimize thermal damage to samples.

Characterization of Particles and Prints: PNCs were characterized using transmission electron microscope (FEI Thermo Glacios) at 200 kV under continuous liquid nitrogen cooling. The structural characterization of printed samples was carried out using a field emission scanning electron microscope (Sigma Zeiss GmbH) equipped with energy-dispersive spectroscope for elemental mapping. Before imaging, the samples were coated with a thin layer of gold (8 nm) using a sputter coater. Imaging was conducted in high vacuum mode with an acceleration voltage of 5 kV. The PANalytical XPert Powder system was utilized for X-ray diffraction (XRD) analysis, employing Cu-Kα wavelength. The measurements were carried out at a power setting of 45 kV and 40 mA at a 2θ range from 0° to 50° with scan speed of 1° per min. All samples used for XRD analysis were in a dry state. For PNC samples, freshly prepared PNCs were transferred to a glass dish and placed under vacuum for 45 min. Subsequently, they were dried at room temperature while being ground with a mortar and pestle to facilitate evaporation and refine them into a fine powder. For selected area diffraction, 0.1 mL of freshly prepared PNCs was diluted in 50 mL of ethanol solution and ultrasonicated for 2 min to ensure dispersion. The solution was then dropped onto a TEM grid, and excess solution was carefully removed from the backside using a tissue. The grid was left to dry at room temperature before TEM observation. Measurements were performed using a Thermo Fisher Themis Z aberration-corrected TEM operated at 300 kV. A monochromator was employed to achieve low-dose conditions (1.5 A/m^2). The diffraction pattern was collected under parallel beam conditions with a camera length of 910 mm. The SAXSpoint 2.0 system (Anton Paar GmbH, Graz, Austria) was utilized for SAXS (Small-Angle X-ray Scattering) and WAXS (Wide-Angle X-ray Scattering) measurements, employing a Primux 100 micro-X-ray source operating at full power (45 kV, 30 mA) with Cu-Kα radiation (X-ray wavelength $\lambda = 1.5418$ Å) and a 2D Eiger detector. The measurements were conducted within a q range of (0.0012–12) and were acquired and converted using the SASfit software packages. All measurements were performed at a temperature of 20 °C. UV–vis transmission measurement was performed using quartz cuvettes with a thickness of 0.1 mm (Hellma Analytics). The inks with a PNC content ranging from 0 to 80 wt.% was added to cuvettes and set using OmniCure S1000 prior to measurements.

Statistical Analysis: All experiments were performed in triplicate, and the data were presented as the mean ± standard deviation. All quantitative data were analyzed using one-way analyses of variance with Tukey's significant difference post-hoc tests for multiple comparisons (GraphPad Prism version 10.0.0 for Windows, GraphPad Software, Boston, Massachusetts USA). The difference between groups of $*p < 0.05$ was regarded as statistically significant.

Supporting Information

Supporting Information is available from the Wiley Online Library or from the author.

Acknowledgements

The authors acknowledge the facilities and the scientific and technical assistance of Sydney Analytical, a core research facility at The University of Sydney. The authors would like to thank Dr Jiangtao Qu and Dr Hongwei Liu from Sydney Microscopy & Microanalysis for assisting with electron microscopy experiments. The authors gratefully acknowledge funding from the Australian Research Council (DP220102876) and LE210100156.

Open access publishing facilitated by The University of Sydney, as part of the Wiley - The University of Sydney agreement via the Council of Australian University Librarians.

Conflict of Interest

The authors declare no conflict of interest.

Data Availability Statement

The data that support the findings of this study are available on request from the corresponding author. The data are not publicly available due to privacy or ethical restrictions.

Keywords

3D Printing, bioceramics, biomimicry, calcium phosphates, nanofabrication

Received: September 10, 2024
Revised: February 13, 2025
Published online: February 28, 2025

[1] H. J. Haugen, S. P. Lyngstadaas, F. Rossi, G. Perale, *J. Clin. Periodontol.* **2019**, *46*, 92.
[2] G. F. de Grado, L. Keller, Y. Idoux-Gillet, Q. Wagner, A.-M. Musset, N. Benkirane-Jessel, F. Bornert, D. Offner, *J. Tissue Eng.* **2018**, *9*, 2041731418776819.
[3] P. Janicki, G. Schmidmaier, *Injury* **2011**, *42*, S77.
[4] H. Liu, Q. Wu, S. Liu, L. Liu, Z. He, Y. Liu, Y. Sun, X. Liu, E. Luo, *Biomaterials* **2024**, *304*, 122406.
[5] D. Xiao, J. Zhang, C. Zhang, D. Barbieri, H. Yuan, L. Moroni, G. Feng, *Acta Biomater.* **2020**, *106*, 22.
[6] J. Jeong, J. H. Kim, J. H. Shim, N. S. Hwang, C. Y. Heo, *Biomater. Res.* **2019**, *23*, s40824.
[7] J. Zhang, D. Tong, H. Song, R. Ruan, Y. Sun, Y. Lin, J. Wang, L. Hou, J. Dai, J. Ding, H. Yang, *Adv. Mater.* **2022**, *34*, 1.
[8] L. Wang, X. Zeng, G. Yan, X. Chen, K. Luo, S. Zhou, P. Zhang, J. Li, T.-W. Wong, *Nanoscale* **2021**, *13*, 16680.
[9] X. Li, M. Liu, F. Chen, Y. Wang, M. Wang, X. Chen, Y. Xiao, X. Zhang, *Nanoscale* **2020**, *12*, 7284.
[10] R. Z. LeGeros, *Chem. Rev.* **2008**, *108*, 4742.
[11] E. García-Gareta, M. J. Coathup, G. W. Blunn, *Bone* **2015**, *81*, 112.
[12] A. K. Rajendran, M. S. J. Anthraper, N. S. Hwang, J. Rangasamy, *Mater. Sci. Eng. R Rep.* **2024**, *159*, 100801.
[13] Q. Li, C. Feng, Q. Cao, W. Wang, Z. Ma, Y. Wu, T. He, Y. Jing, W. Tan, T. Liao, J. Xing, X. Li, Y. Wang, Y. Xiao, X. Zhu, X. Zhang, *Regen. Biomater.* **2023**, *10*, rbad013.
[14] Y. Gou, K. Qi, Y. Wei, Z. Gu, H. Xie, *Nano. TransMed.* **2024**, *3*, 100033.
[15] X. Li, Y. Wang, F. Chen, X. Chen, Y. Xiao, X. Zhang, *Mater. Des.* **2022**, *216*, 110581.
[16] H. Yuan, H. Fernandes, P. Habibovic, J. de Boer, A. M. C. Barradas, A. de Ruiter, W. R. Walsh, C. A. van Blitterswijk, J. D. de Bruijn, *Proc. Natl. Acad. Sci.* **2010**, *107*, 13614.
[17] A. Barba, A. Diez-Escudero, Y. Maazouz, K. Rappe, M. Espanol, E. B. Montufar, M. Bonany, J. M. Sadowska, J. Guillem-Marti, C. Öhman-Mägi, C. Persson, M.-C. Manzanares, J. Franch, M.-P. Ginebra, *ACS Appl. Mater. Interfaces* **2017**, *9*, 41722.
[18] O. Chan, M. J. Coathup, A. Nesbitt, C.-Y. Ho, K. A. Hing, T. Buckland, C. Campion, G. W. Blunn, *Acta Biomater.* **2012**, *8*, 2788.
[19] V. P. Galván-Chacón, P. Habibovic, *Adv. Healthcare Mater.* **2017**, *6*, 1601478.
[20] D. lenihouannen, G. Daculsi, A. Saffarzadeh, O. Gauthier, S. Delplace, P. Pilet, P. Layrolle, *Bone* **2005**, *36*, 1086.
[21] Y. Hong, H. Fan, B. Li, B. Guo, M. Liu, X. Zhang, *Mater. Sci. Eng. R Rep.* **2010**, *70*, 225.
[22] I. Roohani, E. Newsom, H. Zreiqat, *Int. Mater. Rev.* **2023**, *68*, 1075.
[23] M. Bohner, R. J. Miron, *Mater. Today* **2018**, *22*, 132.
[24] R. J. Miron, M. Bohner, Y. Zhang, D. D. Bosshardt, *Periodontol 2000* **2024**, *94*, 9.
[25] Q. Zhang, X. Wang, M. Yang, D. Xu, *J. Mech. Behav. Biomed. Mater.* **2024**, *151*, 106385.
[26] H. Gao, B. Ji, I. L. Jäger, E. Arzt, P. Fratzl, *Proc. Natl. Acad. Sci. U.S.A.* **2003**, *100*, 5597.
[27] H. Gao, S. Chen, *J. Appl. Mech. Trans. ASME* **2005**, *72*, 732.
[28] X. W. Gu, M. Jafary-Zadeh, D. Z. Chen, Z. Wu, Y.-W. Zhang, D. J. Srolovitz, J. R. Greer, *Nano Lett.* **2014**, *14*, 5858.
[29] J. Bauer, L. R. Meza, T. A. Schaedler, R. Schwaiger, X. Zheng, L. Valdevit, *Adv. Mater.* **2017**, *29*, 1701850.
[30] C. Crook, J. Bauer, A. Guell Izard, C. Santos de Oliveira, J. Martins de Souza e Silva, J. B. Berger, L. Valdevit, *Nat. Commun.* **2020**, *11*, 1579.
[31] B. Cantaert, E. Beniash, F. C. Meldrum, *Chem – A Eur J* **2013**, *19*, 14918.
[32] E. Colaço, D. Lefèvre, E. Maisonhaute, D. Brouri, C. Guibert, C. Dupont-Gillain, K. El Kirat, S. Demoustier-Champagne, J. Landoulsi, *Nanoscale* **2020**, *12*, 10051.
[33] E. Colaço, C. Guibert, J. Lee, E. Maisonhaute, D. Brouri, C. Dupont-Gillain, K. El Kirat, S. Demoustier-Champagne, J. Landoulsi, *Biomacromolecules* **2021**, *22*, 3460.
[34] F. Zhang, L. Zhu, Z. Li, S. Wang, J. Shi, W. Tang, N. Li, J. Yang, *Addit. Manuf.* **2021**, *48*, 102423
[35] M.-M. Germaini, S. Belhabib, S. Guessasma, R. Deterre, P. Corre, P. Weiss, *Prog. Mater. Sci.* **2022**, *130*, 100963.
[36] Q. Zhou, X. Su, J. Wu, X. Zhang, R. Su, L. Ma, Q. Sun, R. He, *ACS Biomater. Sci. Eng.* **2023**, *9*, 1164.
[37] B. H. Cumpston, S. P. Ananthavel, S. Barlow, D. L. Dyer, J. E. Ehrlich, L. L. Erskine, A. A. Heikal, S. M. Kuebler, I.-Y. S. Lee, D. McCord-Maughon, J. Qin, H. Röckel, M. Rumi, X.-L. Wu, S. R. Marder, J. W. Perry, *Nature* **1999**, *398*, 51.
[38] M. Carlotti, V. Mattoli, *Small* **2019**, *15*, 1902687.
[39] P. Colombo, G. Franchin, *Nat. Mater.* **2021**, *20*, 1454.
[40] X. Wen, B. Zhang, W. Wang, F. Ye, S. Yue, H. Guo, G. Gao, Y. Zhao, Q. Fang, C. Nguyen, X. Zhang, J. Bao, J. T. Robinson, P. M. Ajayan, J. Lou, *Nat. Mater.* **2021**, *20*, 1506.
[41] J. C. Sänger, B. R. Pauw, B. Riechers, A. Zocca, J. Rosalie, R. Maaß, H. Sturm, J. Günster, *Adv. Mater.* **2023**, *35*, 2208653.
[42] L. Brigo, J. E. M. Schmidt, A. Gandin, N. Michieli, P. Colombo, G. Brusatin, *Adv. Sci.* **2018**, *5*.
[43] J. Bauer, A. Schroer, R. Schwaiger, O. Kraft, *Nat. Mater.* **2016**, *15*, 438.
[44] Z. C. Eckel, C. Zhou, J. H. Martin, A. J. Jacobsen, W. B. Carter, T. A. Schaedler, *Science (80-)* **2016**, *351*, 58.
[45] D. G. Moore, L. Barbera, K. Masania, A. R. Studart, *Nat. Mater.* **2020**, *19*, 212.
[46] L. R. Meza, S. Das, J. R. Greer, *Science, (80-)* **2014**, *345*, 1322.
[47] J. Bauer, S. Hengsbach, I. Tesari, R. Schwaiger, O. Kraft, *Proc. Natl Acad. Sci.* **2014**, *2*, 453.
[48] D. W. Yee, M. L. Lifson, B. W. Edwards, J. R. Greer, *Adv. Mater.* **2019**, *31*, 1901345.
[49] W. Zhang, Z. Li, R. Dang, T. T. Tran, R. A. Gallivan, H. Gao, J. R. Greer, *Nano Lett.* **2023**, *23*, 8162.
[50] S. Ma, W. Bai, D. Xiong, G. Shan, Z. Zhao, W. Yi, J. Wang, *Angew. Chemie. Int. Ed.* **2024**, *63*, 202405135.
[51] H. Hu, C. Deng, H. Gao, T. Han, S. Xue, Y. Tang, M. Zhang, M. Li, H. Liu, L. Deng, W. Xiong, *Adv. Mater.* **2024**, *36*, 2405053.
[52] F. Han, S. Gu, A. Klimas, N. Zhao, Y. Zhao, S.-C. Chen, *Science (80-)* **2022**, *378*, 1325.
[53] J. Tang, H. Liang, A. Ren, L. Ma, W. Hao, Y. Yao, L. Zheng, H. Li, Q. Li, *Adv. Mater.* **2024**, *36*, 2400080.
[54] Q. Li, J. Kulikowski, D. Doan, O. A. Tertuliano, C. J. Zeman, M. M. Wang, G. C. Schatz, X. W. Gu, *Science (80-)* **2022**, *378*, 768.
[55] J. Tang, N. Xu, A. Ren, L. Ma, W. Xu, Z. Han, Z. Chen, Q. Li, *Angew. Chemie. Int. Ed.* **2024**, *63*, 202403645.
[56] W. J. E. M. Habraken, J. Tao, L. J. Brylka, H. Friedrich, L. Bertinetti, A. S. Schenk, A. Verch, V. Dmitrovic, P. H. H. Bomans, P. M. Frederik, J.

Laven, P. van der Schoot, B. Aichmayer, G. de With, J. J. DeYoreo, N. A. J. M. Sommerdijk, *Nat. Commun.* **2013**, *4*, 1507.
[57] D. Gebauer, *Science (80-)* **2008**, *120*, 1819.
[58] S. Yao, Y. Xu, Y. Zhou, C. Shao, Z. Liu, B. Jin, R. Zhao, H. Cao, H. Pan, R. Tang, *ACS Appl. Bio Mater.* **2019**, *2*, 4408.
[59] S. Yao, Z.-A. Xie, L. Ye, B. Jin, Y. Xu, M. Wang, C. Yu, R. Tang, X. Fang, S. Fan, *Mater. Today Nano.* **2023**, *21*, 100290.
[60] S. Boonrungsiman, E. Gentleman, R. Carzaniga, N. D. Evans, D. W. McComb, A. E. Porter, M. M. Stevens, *Proc. Natl. Acad. Sci. U.S.A.* **2012**, *109*, 14170.
[61] A. Dey, P. H. H. Bomans, F. A. Müller, J. Will, P. M. Frederik, G. de With, N. A. J. M. Sommerdijk, *Nat. Mater.* **2010**, *9*, 1010.
[62] A. Lotsari, A. K. Rajasekharan, M. Halvarsson, M. Andersson, *Nat. Commun.* **2018**, *9*, 4170.
[63] Y.-X. Ma, S. E. Hoff, X.-Q. Huang, J. Liu, Q.-Q. Wan, Q. Song, J.-T. Gu, H. Heinz, F. R. Tay, L.-N. Niu, *Acta Biomater.* **2021**, *120*, 213.
[64] K. He, M. Sawczyk, C. Liu, Y. Yuan, B. Song, R. Deivanayagam, A. Nie, X. Hu, V. P. Dravid, J. Lu, C. Sukotjo, Y.-P. Lu, P. Král, T. Shokuhfar, R. Shahbazian-Yassar, *Sci. Adv.* **2020**, *6*, eaaz7524.
[65] A. Lotsari, A. K. Rajasekharan, M. Halvarsson, M. Andersson, *Nat. Commun.* **2018**, *9*, 4170.
[66] L. M. Epasto, T. Georges, A. Selimović, J.-M. Guigner, T. Azaïs, D. Kurzbach, *Anal. Chem.* **2021**, *93*, 10204.
[67] X. Yang, C. Zhang, X. Yang, Z. Xu, *J. Mol. Liq.* **2023**, *378*, 121585.
[68] B. Jin, Z. Liu, C. Shao, J. Chen, L. Liu, R. Tang, J. J. De Yoreo, *Cryst. Growth Des.* **2021**, *21*, 5126.
[69] J. Wu, Y.-Q. Chi, Y.-J. Yan, M.-Z. Ji, X. Chen, X.-Q. Yang, Y. Gao, Q. Zou, L. Zou, X.-Y. Li, *Nanoscale* **2023**, *15*, 3940.
[70] Q. Liu, T. Li, S. W. Gan, S. Y. Chang, C. C. Yen, W. Zhai, *Addit. Manuf.* **2023**, *61*, 103332.
[71] O. Chan, M. J. Coathup, A. Nesbitt, C.-Y. Ho, K. A. Hing, T. Buckland, C. Campion, G. W. Blunn, *Acta Biomater.* **2012**, *8*, 2788.
[72] K. Zhang, Y. Fan, N. Dunne, X. Li, *Regen Biomater* **2018**, *5*, 115.
[73] S. G. Higgins, M. Becce, A. Belessiotis-Richards, H. Seong, J. E. Sero, M. M. Stevens, *Adv. Mater.* **2020**, *32*, 1903862.
[74] C. Chiappini, Y. Chen, S. Aslanoglou, A. Mariano, V. Mollo, H. Mu, E. De Rosa, G. He, E. Tasciotti, X. Xie, F. Santoro, W. Zhao, N. H. Voelcker, R. Elnathan, *Nat. Protoc.* **2021**, *16*, 4539.
[75] Q. He, T. Tang, Y. Zeng, N. Iradukunda, B. Bethers, X. Li, Y. Yang, *Adv. Funct. Mater.* **2024**, *34*, 2309323.
[76] S.-M. Wen, S.-M. Chen, W. Gao, Z. Zheng, J.-Z. Bao, C. Cui, S. Liu, H.-L. Gao, S.-H. Yu, *Adv. Mater.* **2023**, *35*, 2211175.